



1 **Critical Role of Dust Induced Electrostatic Coagulation in the Evolution** 2 **of Aerosol Size Distributions in the Atmosphere**

3 Luoqiu Quan¹, Ruoyu Zhang¹, Gui Dai¹, Xinghua Jiang¹, Xiangyang Wang¹, Xiewen Ma¹, Xinyu Liu¹,
4 Qianqian Gao¹, Xiaohui Lu^{1*}, Xiaofei Wang^{1,2,3*}

5 ¹Department of Environmental Science and Engineering, Shanghai Key Laboratory of Atmospheric Particle Pollution and
6 Prevention, Fudan University, Shanghai 200433, China.

7 ²Shanghai Institute of Pollution Control and Ecological Security, Shanghai 200092, China.

8 ³Fudan Zhangjiang Institute, Shanghai 201203, China.

9 *Correspondence to:*

10 Xiaofei Wang (xiaofeiwang@fudan.edu.cn)

11 Xiaohui Lu (luxiaohui@fudan.edu.cn)

12 **Abstract.** Coagulation modifies the particle size distributions (PSD) of atmospheric aerosols, affecting their
13 optical properties, cloud droplet activation, and gravitational deposition. While Coulomb forces may impact
14 coagulation processes between charged aerosols, such as dust, most coagulation models neglect the effects
15 of aerosol charge. Here, we address the lack of single-particle charge measurements for dust aerosols by
16 developing a method to retrieve their joint size-charge distributions. By incorporating aerosol charge into the
17 coagulation kernel, simulations in a dust-only scenario at typical environmental concentrations show that, on
18 hourly timescales, electrostatic force leads to a reduction of up to ~64% in number concentration relative to
19 Brownian coagulation. Moreover, electrostatic coagulation between dust and ambient sub-500 nm aerosols
20 modifies the latter's PSD by ~10% compared with Brownian coagulation. These results strongly suggest that
21 electrostatic coagulation should be considered in air quality models.

22 **1 Introduction**

23 Changes in the aerosol particle size distribution (PSD) alter aerosol optical properties and deposition behavior.
24 These changes affect atmospheric radiation, cloud droplet activation, and aerosol removal processes (Tegen
25 et al., 1996; Pöschl, 2005). One important driver of PSD evolution is coagulation. Coagulation shifts aerosols
26 toward larger sizes and reduces the total number concentration. Quantifying PSD evolution due to
27 coagulation is essential for assessing atmospheric effects. Aerosol coagulation can be driven by Brownian
28 motion, van der Waals and Coulomb interactions, and hydrodynamic (shear/turbulence-induced) processes.
29 Different mechanisms lead to different coagulation kernels and thus distinct PSD evolution (Seinfeld et al.,
30 2016).

31 Most widely used coagulation models use Brownian coagulation as the fundamental mechanism and include
32 no explicit charge terms in the coagulation kernel (Lee et al., 2009; Ramnarine et al., 2019; Grell et al., 2005).
33 When aerosols carry charge, Coulomb forces alter aerosol collision and coalescence processes. Oppositely



34 charged aerosols experience Coulomb attraction and collide more frequently, whereas like-charged aerosols
35 experience Coulomb repulsion and collide less often (Harrison and Carslaw, 2003). Experimental and
36 numerical studies show that when aerosols carry large opposite charges or the charge distribution is highly
37 asymmetric, the electrostatic coagulation rate is significantly higher than the Brownian coagulation rate
38 (Adachi et al., 1981). Therefore, using such Brownian models to assess the coagulation of highly charged
39 atmospheric aerosols may introduce bias for charged aerosols. Explicit consideration of Coulomb interactions
40 in the coagulation process is necessary to improve the accuracy of modeled PSD evolution.

41 Highly charged aerosols are common in the atmosphere, typically including dust aerosols, volcanic ash, sea
42 spray, and urban coarse aerosols (Harrison and Carslaw, 2003; Cimarelli and Genareau, 2022). Dust aerosols
43 with geometric diameters up to 20 μm have an emission of approximately 5000 Tg yr^{-1} and possess long-
44 range transport capability (Kok et al., 2021). These features produce significant environmental effects by
45 influencing atmospheric radiative forcing and cloud condensation nuclei (CCN) number concentration.
46 Meanwhile, the PSD of dust aerosols strongly influences their radiative properties, CCN concentration, and
47 deposition rate (Tegen et al., 1996; Lee et al., 2009). Thus, dust aerosols are a highly representative system
48 for investigating coagulation processes in highly charged aerosol populations. Quantifying the evolution of
49 the PSD of dust aerosols during coagulation is essential for improving such assessments. Based on physics-
50 based numerical calculations, Mallios et al. (2022) predicted mean net dust aerosol charges of approximately
51 0.5 – 2000 e, exceeding those expected under Boltzmann equilibrium. The existence of such charge states
52 suggests that electrostatic interactions may become non-negligible, highlighting the potential importance of
53 electrostatic coagulation in dust aerosol systems (Adachi et al., 1981). The specific differences between
54 electrostatic and Brownian coagulation of dust aerosols in driving the PSD evolution of ambient aerosols in
55 dust-laden environments are not yet well understood.

56 Techniques for measuring single-particle charges on dust aerosols are required to quantify PSD evolution
57 driven by electrostatic coagulation. Such techniques must provide polarity discrimination and size-resolved
58 precision. Existing approaches can be broadly classified into three categories: bulk net-charge measurements
59 (e.g., Faraday-cup or induction electrometry), single-particle trajectory or deflection measurements, and
60 high-precision single-particle instruments based on levitation or trapping (e.g., electrodynamic balance;
61 Zhang et al., 2020; Li et al., 2022). These methods usually deliver only some of the above capabilities—
62 rarely all at once, especially in high-throughput, in situ settings. Obtaining single-particle charge
63 measurements for dust aerosols that are directly applicable to electrostatic coagulation modeling remains a
64 major technical challenge.



65 The core objective of this study is to quantify the differences between electrostatic and Brownian coagulation
66 of dust aerosols in driving the PSD evolution of ambient aerosols during dust events. To address this objective,
67 we develop a new method to obtain single-particle charge values of dust aerosols that can be directly used
68 for electrostatic coagulation modeling by means of laboratory measurements and computational inversion.
69 The measured charges serve as initial conditions for subsequent coagulation simulations, and the method
70 provides a reusable workflow for related research. Based on the comparative simulation results, the role of
71 explicit charge inclusion in coagulation modeling is evaluated.

72 **2 Materials and Methods**

73 This section describes the measurements, data processing, and coagulation model. The PSDs and electrical
74 mobility diameter distributions of laboratory-generated dust aerosols were obtained from measurements,
75 while single-particle charge distributions were derived from measurements and computational inversion. The
76 PSDs of ambient sub-500 nm aerosols were obtained from field measurements, and their charge distributions
77 were obtained through computation. The number concentrations of dust aerosols, with or without ambient
78 sub-500 nm aerosols, were mapped onto a common size-charge matrix and used as model initial conditions.
79 The model simulated Brownian and electrostatic coagulation and updated the aerosol number concentration
80 matrix over time.

81 **2.1 Laboratory Dust Aerosol Generation**

82 **2.1.1 Soil Samples**

83 This study used eight soil samples to produce laboratory-generated dust aerosols. Two were collected from
84 the Dunhuang dust source area, Gansu Province, China (S1, S2). Three were collected from the Inner
85 Mongolia dust source area (Ulanqab and Hohhot), China (S3–S5). Three were collected from non-dust-source
86 areas in Qingxi Country Park, Shanghai (S6), Fudan University’s Jiangwan Campus, Shanghai (S7), and
87 Baoshi Town in Anju District, Suining, Sichuan Province (S8). All samples were passed through a 100 mesh
88 nylon sieve to remove coarse particles and organic debris. Site coordinates and soil texture are listed in Table
89 S1.

90 **2.1.2 Dust Aerosol Generator**

91 A dust aerosol generator (SyGAVib) was used to produce laboratory-generated dust aerosols (Qu et al., 2020).
92 The device consists of a cylindrical acrylic chamber, a loudspeaker, and an aluminum cup with an open top.
93 Operating parameters were set following Qu et al. (2020) to generate a stable dust plume. Each experiment
94 used 0.3 g of soil placed in the aluminum cup, with the cup fixed to the loudspeaker diaphragm. The
95 loudspeaker was driven at 100 Hz with medium output power to loosen particles via collisions. Three bottom



96 inlet ports supplied dried and filtered air at a total flow rate of 8 liters per minute (LPM). The two lower side
97 ports each supplied 3.5 LPM of sheath air to provide upward momentum, and the port above the cup delivered
98 air of 1 LPM into the cup to simulate turbulence and loft the dust aerosols. To avoid the effect of humidity
99 on Coulomb forces between aerosols (Ma et al., 2023), the plume relative humidity was maintained at 25–
100 35%. A temperature-humidity probe was placed at the top of the chamber. The setup is shown in Figure S1.

101 **2.2 Dust Aerosol Measurements**

102 **2.2.1 Size and Electrical Mobility Distributions**

103 Size distributions of dust aerosols were measured with an Aerodynamic Particle Sizer (APS, TSI Inc. Inlet
104 flow rate: 1 LPM) over 0.5–20 μm , whereas aerosols $< 0.5 \mu\text{m}$ were measured with a Scanning Mobility
105 Particle Sizer (SMPS, TSI Inc. Sampling flow rate: 0.3 LPM). For consistency, all aerosol sizes were
106 converted to electrical mobility diameter, which more accurately approximates the geometric diameter of
107 non-spherical aerosols. The detailed conversion formula is provided in Equation (3). Electrical mobility
108 distributions were measured with an SMPS without a neutralizer, covering $1.56 \times 10^{-9} - 1.07 \times 10^{-6} \text{ m}^2 \cdot \text{V}^{-1} \cdot \text{s}^{-1}$.
109 The schematic is in Figure S1.

110 **2.2.2 Single-Particle Charge Measurement**

111 The experimental setup is shown in Figure 1. The laboratory-generated dust aerosols were then directed into
112 the Differential Mobility Analyzer (DMA, Models 3080 and 3082, TSI Inc., inlet flow rate: 1 LPM) at
113 prescribed electrical mobilities Z_p (Table S2), and the aerodynamic diameter of the classified aerosols was
114 measured with an APS. The single-particle charge distribution was retrieved through joint analysis of the set
115 electrical mobility and the electrical mobility diameter (D_p).

116 Electrical mobility equation:

$$117 \quad Z_p = \frac{neC}{3\pi\mu D_p} \quad (1)$$

118 Z_p is the electrical mobility ($\text{m}^2/\text{v}\cdot\text{s}$), n is the single-particle charge, e is the elementary charge ($1.6 \times 10^{-19} \text{ C}$),
119 π is the circular constant, and μ is the dynamic viscosity of air ($1.85 \times 10^{-5} \text{ Pa}\cdot\text{s}$ at $25 \text{ }^\circ\text{C}$), D_p is the electrical
120 mobility diameter (m).

121 where C is the Cunningham slip correction factor, calculated as:



122
$$C = 1 + \frac{2\lambda}{D} \left[1.257 + 0.4 \exp \left(-\frac{1.1D}{2\lambda} \right) \right] \quad (2)$$

123 D is the particle diameter (m), λ is the molecular mean free path (68×10^{-9} m).

124 The aerodynamic diameter was converted to the electrical mobility diameter using the size conversion
125 relationship (Seinfeld et al., 2016):

126
$$D_p = D_a \sqrt{\chi^3 \frac{\rho_0 C(D_m)^2 C(D_a)}{\rho_p C(D_{ve})^3}} \quad (3)$$

127 is derived from the following two equations:

128
$$\frac{D_p}{C(D_p)} = \frac{D_{ve} \chi}{C(D_{ve})} \quad (4)$$

129
$$D_a = D_{ve} \sqrt{\frac{\rho_p C(D_{ve})}{\chi \rho_0 C(D_a)}} \quad (5)$$

130 χ is the dynamic shape factor under the experimental conditions (set to 1.0 assuming spherical dust aerosols),
131 D_a is the aerodynamic diameter (m), D_{ve} is the volume equivalent diameter (m), ρ_0 is the reference density
132 (1 g/cm^3), and ρ_p is the density of dust aerosol particles, taken as 2.65 g/cm^3 (Haywood et al., 2003a). Missing
133 charge bin concentrations were obtained by linear interpolation along the charge axis.

134 A custom charged particle remover (CPR) operated at 3.5 kV was used to determine the neutral fraction of
135 dust aerosols (Zhang et al., 2023). The CPR consists of two coaxially aligned stainless-steel tubes that create
136 a radial electric field, which removes charged aerosols and allows only neutral aerosols to pass through
137 unaffected (design and operation details in Figure S2).

138 **2.3 Ambient Sub-500 nm Aerosol Size Distribution Measurement and Charge Calculation**

139 The PSD of representative ambient sub-500 nm aerosols was determined from measurements collected during
140 periods without dust events at the seventh floor of the Environmental Science Building, Jiangwan Campus
141 of Fudan University, Shanghai, China, on 30 September 2024. The detailed geographic coordinates of the
142 measurement site are provided in Table 3. Given that ultrafine aerosols ($<100 \text{ nm}$) in urban environments
143 typically contribute the majority of the total number concentration ($>80\%$) (Kumar et al., 2014; Morawska



144 et al., 2008), and that the WMO Global Atmosphere Watch (GAW) multi-site analysis also used the 10 –
145 500 nm size range to represent total number concentration (Rose et al., 2021), the electrical mobility diameter
146 distribution of ambient sub-500 nm aerosols was measured with an SMPS over 14 – 500 nm. The
147 measurement setup is shown in Figure S4. Assuming a natural bipolar ion background (Tigges et al., 2015),
148 aerosol charge states were assumed near Boltzmann equilibrium. The charge distribution for each size bin
149 was computed from the measured size distribution using the Boltzmann formulation (Liu and Pui, 1974;
150 Table S4).

151 **2.4 Coagulation Modeling**

152 **2.4.1 Input Matrix Construction**

153 In the coagulation model, aerosol number concentrations are represented on a unified matrix in size and
154 charge. Dust aerosol model inputs were derived from three Inner Mongolia soil samples. Given that Mongolia
155 accounted for more than 42% of dust concentrations in northern China during March–April 2023 (Chen et
156 al., 2023) and shares a dust source belt and similar emission and transport pathways with Inner Mongolia
157 (Mu and Fiedler, 2025), dust aerosols generated from Inner Mongolia soils are representative. The dataset
158 was discretized on a two-dimensional size-charge matrix, defined by electrical mobility diameter D_p (Table
159 S5) and single-particle charge number $z \in \{-1000, -999, \dots, 999, 1000\}$. The size matrix comprised 131
160 logarithmically spaced bins from 14.1 nm to 7 μm . This yielded three number concentration matrices $N_k(D_p,$
161 $z)$ for $k = 1, 2, 3$. Each N_k was normalized to a joint probability density matrix:

$$162 \quad f_k(D_p, z) = \frac{N_k(D_p, z)}{\sum_{D_p, z} N_k(D_p, z)} \quad (6)$$

163 and the representative joint probability density function was obtained by taking the element-wise arithmetic
164 mean:

$$165 \quad \bar{f}(D_p, z) = \frac{1}{3} \sum_{k=1}^3 f_k(D_p, z) \quad (7)$$

166 Following Chen et al. (2023), the dust aerosol number concentration of $\sim 300 \text{ \#/cm}^3$ ($\sim 3 \text{ mg/m}^3$) observed in
167 Beijing during transport from Mongolia was mapped onto the matrix according to the above representative
168 joint probability density matrix, yielding a representative number concentration matrix of dust aerosols. This
169 matrix was combined with the ambient sub-500 nm aerosol matrix, or used alone, to form the initial mixed



170 field that served as the model input. For sensitivity analysis under dust-only conditions, additional
 171 simulations were performed with initial dust aerosol number concentrations of 50, 100, 200, 300, 500, and
 172 1000 #/cm³ (Figure 4). This range of concentrations was used to evaluate model stability under varying initial
 173 conditions and to examine the concentration dependence of electrostatic coagulation.

174 2.4.2 Brownian Coagulation

175 Under Brownian coagulation, the generation and loss terms are computed on the size matrix for each size bin,
 176 following Zebel (1958) and Oron and Seinfeld (1989a):

$$177 \quad \frac{dN(D_p)}{dt} = \frac{1}{2} \sum_{D_p'} \sum_{D_p''} \beta_{B(D_p', D_p'')} N(D_p') N(D_p'') - N(D_p) \sum_{D_p^*} \beta_{B(D_p, D_p^*)} N(D_p^*) \quad (8)$$

178 N is the aerosol number concentration in a size bin (#/cm³), D_p' and D_p'' are the aerosol diameters (m), D_p^*
 179 denotes the representative size of aerosols colliding with D_p (m), and β_B is the Brownian coagulation kernel
 180 (m³/s), calculated using the Fuchs (1964) formulation at 25 °C.

181 The Brownian coagulation kernel is given by:

$$182 \quad \beta_B = 2\pi(d_1 + d_2)(D_{p1} + D_{p2}) \times \left(\frac{D_{p1} + D_{p2}}{D_{p1} + D_{p2} + 2(\delta_1^2 + \delta_2^2)^{1/2}} + \frac{8(D_1 + D_2)}{(\bar{c}_1^2 + \bar{c}_2^2)^{1/2}(D_{p1} + D_{p2})} \right)^{-1} \quad (9)$$

183 where:

$$184 \quad \bar{c}_i = \left(\frac{8kT}{\pi m_i} \right)^{1/2} \quad (10)$$

$$185 \quad \lambda_i = \frac{8D_i}{\pi \bar{c}_i} \quad (11)$$

$$186 \quad \delta_i = \frac{1}{3D_{pi}\lambda_i} [(D_{pi} + \lambda_i)^3 - (D_{pi}^2 + \lambda_i^2)^{3/2}] - D_{pi} \quad (12)$$

$$187 \quad d_i = \frac{kTC_c}{3\pi\mu D_{pi}} \quad (13)$$

188 D_{pi} is the aerosol diameter (m), k is the Boltzmann constant (1.380649×10^{-23} J·K⁻¹), T is the temperature
 189 (298.15 K), and m_i is the aerosol mass (kg).

190 Coagulation satisfies volume conservation:



191
$$D_p = (D_p^3 + D_p^{*3})^{1/3} \quad (14)$$

192 At each time step a pairwise collision rate matrix is formed. Columns correspond to the size bins being
 193 depleted and rows correspond to the pairing size bins that collide with them. The total coagulation rate for a
 194 given size bin is obtained by summing all elements in its column. The remaining number concentration in
 195 the size bin D_p after one time step is:

196
$$N_{rem}(D_p) = N(D_p) - \Delta t N(D_p) \sum_{D_p^*} \beta_B(D_p, D_p^*) N(D_p^*) \quad (15)$$

197 The time step Δt was 1 s for 0–100 s, 10 s for 100–1000 s, and 100 s for 1000–10000 s.

198 For the formation term, the upper-triangular part of the rate matrix was used to avoid double counting. For
 199 each pair in the upper triangle of the pairwise collision rate matrix, the equivalent product size was computed
 200 from volume conservation and mapped to the nearest discrete size bin. The number of newly formed aerosols
 201 was then added to the corresponding product bin. After traversing the upper triangle, the formation term for
 202 each size bin was obtained. The field $N(D_p)$ was updated by adding the formation matrix to the remaining
 203 concentration matrix.

204 2.4.3 Electrostatic Coagulation

205 Electrostatic coagulation was modeled using the Brownian framework with a Coulomb correction applied to
 206 the coagulation kernel:

207
$$\begin{aligned} \frac{dN(D_p, z)}{dt} = & \frac{1}{2} \sum_{D_p'} \sum_{D_p''} \sum_{z'=-1000}^z \beta_{E(D_p', z-z'), (D_p'', z')} N(D_p', z-z') N(D_p'', z') \\ & - N(D_p, z) \sum_{D_p^*} \sum_{z^*} \beta_{E(D_p, z), (D_p^*, z^*)} N(D_p^*, z^*) \end{aligned} \quad (16)$$

208 β_E is the electrostatic coagulation kernel (m^3/s), derived from the Brownian kernel with a Coulomb
 209 interaction correction. In this study, all parameters were set to 25 °C. z' denotes particles with charge
 210 number smaller than z , and z^* denotes the representative charge of aerosols colliding with z .

211 The electrostatic coagulation kernel is given by (Brownian kernel with Coulomb correction):

212
$$\beta_E = \frac{\beta_B}{W_C} \quad (17)$$



213
$$W_c = \frac{e^\kappa - 1}{\kappa} \quad (18)$$

214
$$\kappa = \frac{z_1 z_2 e^2}{4\pi \epsilon_0 \epsilon (R_{p1} + R_{p2}) kT} \quad (19)$$

215 z_i is the aerosol charge number, e is the elementary charge ($1.60217662 \times 10^{-19}$ C), $\epsilon_0 \epsilon$ is the dielectric
216 permittivity of air (8.854737×10^{-12} F/m), and R_{pi} is the aerosol effective radius (m).

217 Simulating electrostatic coagulation requires accounting for atmospheric ions. Dust aerosols are typically
218 transported at altitudes of ~2–5 km, where they are influenced by cosmic-ray ionization (Kok et al., 2021;
219 Xie et al., 2022). The initial ion number concentration is 440 #/cm³ and the ion production rate is 2 #/cm³·s
220 (Tammet et al., 2006; Israel et al., 1970, 1973; Hoppel et al., 1986a). At each time step, the ion balance and
221 aerosol charging are updated first and coagulation is then applied.

222 The pairwise collision rate matrix in electrostatic coagulation is indexed by paired size and charge (D_p, z).
223 As in Brownian coagulation, the loss for any source cell is obtained by summing the column of the pairwise
224 collision rate matrix corresponding to that cell. The formation term differs in that the product is indexed by
225 both size and charge. The size of newly formed aerosols is computed from volume conservation and mapped
226 to the nearest discrete size bin. The charge of newly formed aerosols is computed from charge conservation
227 and assigned to the corresponding integer charge bin. The resulting size and charge indices are then used to
228 add the newly formed aerosols to the corresponding matrix cell.

229 It should be noted that certain features of the coagulation model may introduce slight biases. The calculation
230 of the size of the product aerosol follows volume conservation and the computed size may deviate from the
231 true volume-equivalent diameter because aerosols are not ideal spheres. Moreover, although a relatively fine
232 size discretization is adopted, binning still introduces errors, which are more apparent when the size
233 difference between dust aerosols and ambient sub-500 nm aerosols is large. Coagulation products are often
234 binned near the size of the larger precursor aerosol. This underestimates the contribution of small aerosols,
235 slightly reduces total aerosol volume, and subtly shifts the PSD toward smaller sizes. These small biases
236 should be considered when interpreting quantitative results.

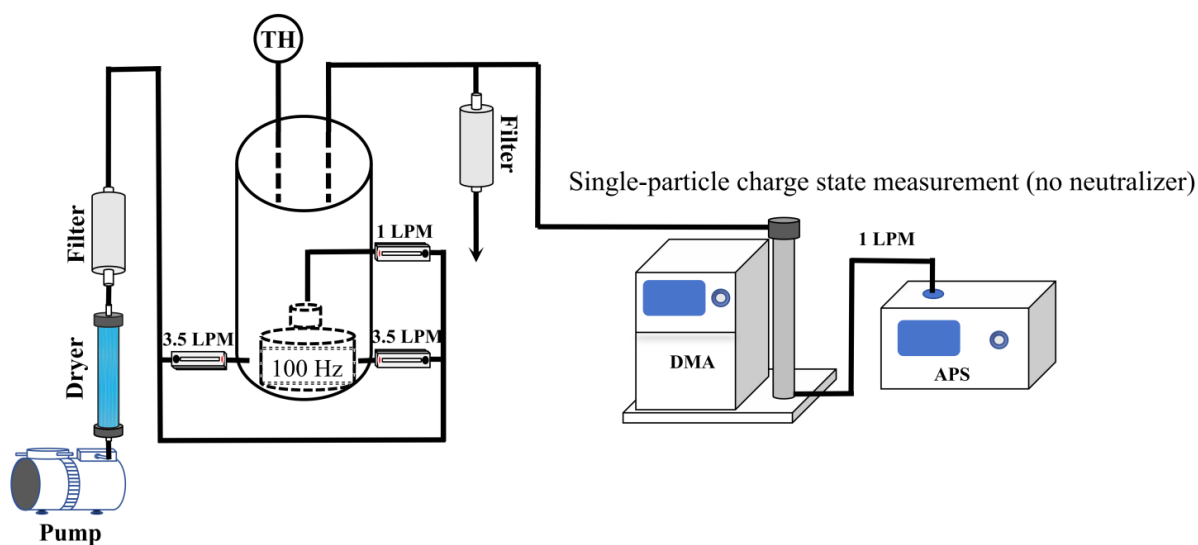
237 **3 Results and Discussion**

238 **3.1 Size and charge characteristics of laboratory-generated dust aerosols**

239



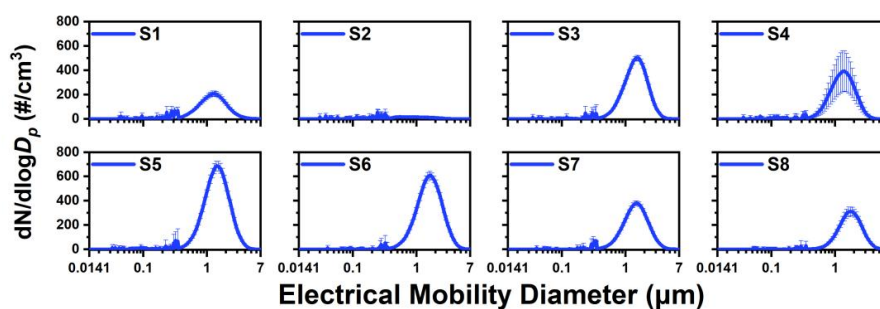
240 This study used a DMA – APS measurement system combined with inversion of the electrical mobility
241 equation to obtain size-resolved single-particle charge distributions of individual dust aerosol particles. The
242 experimental setup is shown in Figure 1. These measurements provide the basis for subsequent size – charge
243 coupled analyses and coagulation simulations, and enable a standardized workflow for in situ measurement
244 of charged dust aerosols.



245

246 **Figure 1.** Schematic of the experimental workflow for measuring single-particle charge.

247 The laboratory-generated dust aerosols are shown to be representative of real atmospheric dust (Shao et al.,
248 2016). Figure 2 shows that the peak diameters of the eight dust aerosol samples fall within 1 – 3 μm ,
249 consistent with long-range transported atmospheric dust aerosols (Maring et al., 2003). This size distribution
250 also agrees well with field APS measurements of transported dust in Yinchuan, China, further supporting the
251 atmospheric representativeness of the laboratory-generated aerosols (Shao and Mao, 2016). Investigating
252 coagulation within this size range therefore provides greater atmospheric relevance.

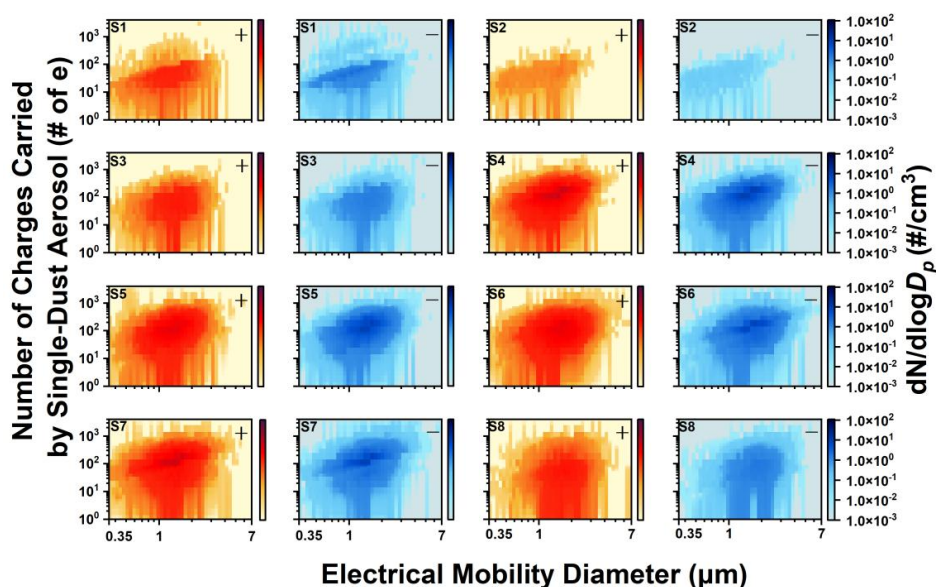


253



254 **Figure 2.** Particle size distributions of dust aerosol samples S1–S8 from 23 nm to 10 μm .

255 The data in Figure 3 indicate that the charge distribution of the laboratory-generated dust aerosols spans a
256 range of ~ 10 –1000 e , with a peak around 100 e . These values are much higher than those at the bipolar
257 Boltzmann equilibrium. The distributions are nearly symmetric between positive and negative charges,
258 indicating no pronounced polarity preference. This near-symmetric bipolar character is further supported by
259 the nearly identical positive and negative electrical mobility distributions in Figure S5. These measurements
260 directly resolve the size-dependent charge distribution of individual dust aerosols, providing observational
261 constraints that are typically unavailable in coagulation studies. This nonequilibrium bipolar charge
262 distribution enhances Coulomb interactions and consequently leads to a higher coagulation rate (Adachi et
263 al., 1981).



264

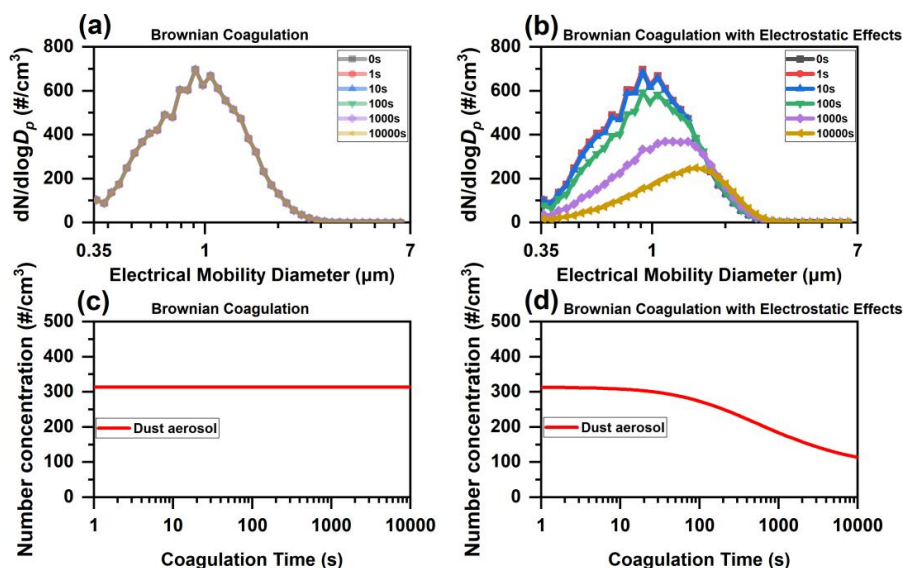
265 **Figure 3.** Maps of the joint distribution of number of charges carried by single-dust aerosol and aerodynamic
266 diameter for dust aerosol samples S1–S8. The x axis is electrical mobility diameter on a logarithmic scale
267 from 0.7–12.5 μm . The y axis is the number of elementary charges per aerosol on a logarithmic scale from
268 1–4000 e . Color encodes number concentration on a logarithmic scale from 10^{-3} – 10^2 $\#/\text{cm}^3$. Red indicates
269 positively charged aerosols and blue indicates negatively charged aerosols.

270 **3.2 PSD evolution of dust aerosols in dust-only scenario under Brownian and electrostatic coagulation**



271 The PSD evolution under electrostatic coagulation of dust aerosols differs significantly from that under
272 Brownian coagulation. The size-charge number concentration matrix of dust aerosols was used as the model
273 input, with an initial total number concentration of 300 \#/cm^3 . This value was chosen to represent a
274 characteristic peak in dust number concentrations commonly observed under non-extreme dust conditions in
275 northern China, based on long-term measurements in Beijing and nearby regions (Chen et al., 2023). The
276 choice of dust aerosol number concentration is described in Methods Section 2.4.1.

277 The PSD evolution under Brownian and electrostatic coagulation from 0 to 10000 s was then simulated, as
278 shown in Figure 4. From 0 to 10000 s, the PSD is essentially unchanged under Brownian coagulation (Figure
279 4a), whereas under electrostatic coagulation the peak diameter shifts from ~ 0.9 to $1.5 \mu\text{m}$ and the peak
280 number concentration falls from ~ 700 to 250 \#/cm^3 (Figure 4b). These results show that dust aerosols change
281 the PSD on hourly timescales through electrostatic coagulation. Therefore, calculations of coagulation
282 processes involving highly charged aerosols should explicitly account for the influence of Coulomb forces.

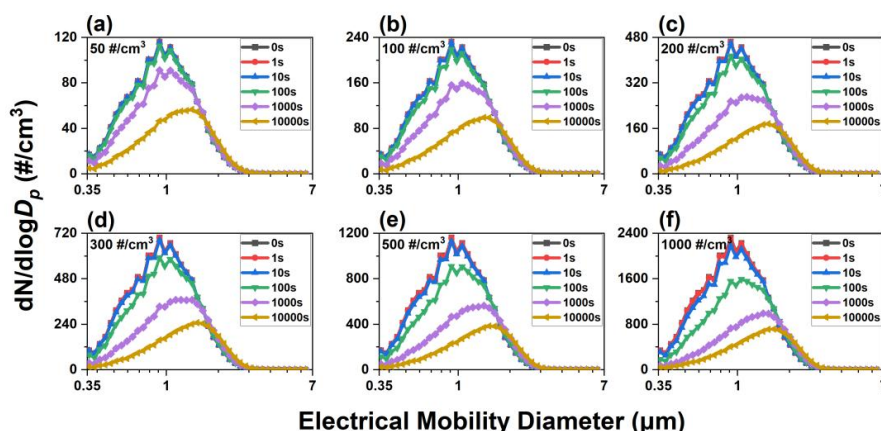


283

284 **Figure 4.** Temporal evolution of the PSD and total number concentration for dust aerosols (dust-only with
285 an initial concentration at 300 \#/cm^3), simulated at $25 \text{ }^\circ\text{C}$. (a) Dust aerosols' PSD under Brownian coagulation,
286 remaining essentially unchanged. (b) Dust aerosols' PSD under electrostatic coagulation. (c) Total aerosol
287 number concentration under Brownian coagulation. (d) Same as (c), but for electrostatic coagulation.

288 In addition, sensitivity tests of dust-only electrostatic coagulation with initial dust aerosol number
289 concentrations from 50 to 1000 \#/cm^3 (Figure 5) show that the qualitative features of PSD evolution remain

290 consistent across this concentration range. The simulations further show that higher initial dust aerosol
291 number concentrations experience a stronger decrease in the PSD peak over 0–10000 s. This behavior is
292 consistent with coagulation kinetics, where the collision frequency scales with the square of the number
293 concentration ($dN/dt \propto -KN^2$; Seinfeld et al., 2016). This effect is likely to occur in dense dust plumes or
294 severe dust-storm events in the real atmosphere.



295

296 **Figure 5.** Temporal evolution of the PSD due to electrostatic coagulation under dust-only conditions at
297 different initial number concentrations at 25 °C. (a) 50 #/cm³; (b) 100 #/cm³; (c) 200 #/cm³; (d) 300 #/cm³;
298 (e) 500 #/cm³; (f) 1000 #/cm³. The corresponding temporal evolution of aerosol charge distributions is shown
299 in Figures S6–S11.

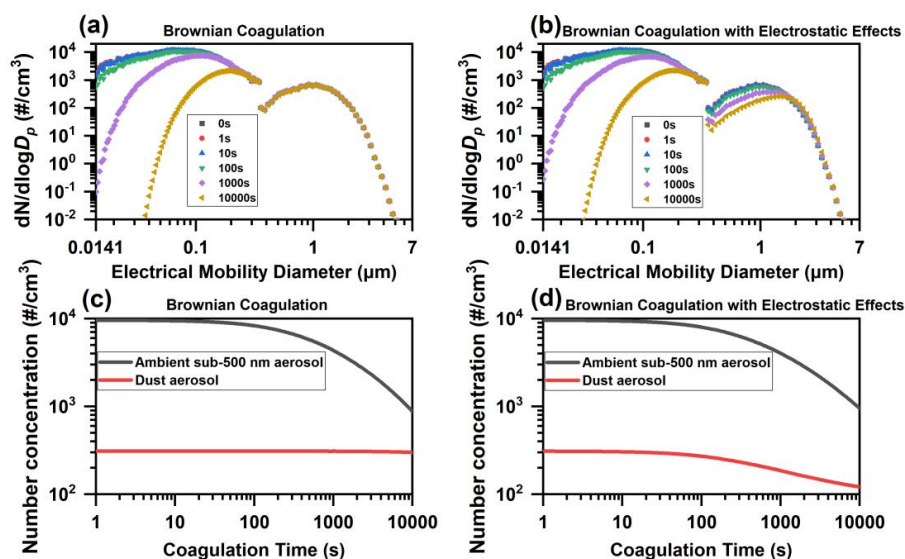
300 **3.3 PSD evolution of ambient aerosols containing a dust fraction of 300 #/cm³ under Brownian and** 301 **electrostatic coagulation**

302 This section examines the PSD evolution of ambient aerosols containing a dust fraction of 300 #/cm³ under
303 Brownian and electrostatic coagulation using a mixed aerosol system. The model input consisted of the PSD
304 and charge information for (1) ambient sub-500 nm aerosols assuming a Boltzmann-equilibrium charge
305 distribution, and (2) dust aerosols with a total number concentration of 300 #/cm³. These inputs were used to
306 simulate PSD evolution under Brownian and electrostatic coagulation from 0 to 10000 s. Comparison with a
307 dust-only scenario indicates that dust PSD evolution remains essentially unchanged under both Brownian
308 and electrostatic coagulation over 0–10,000 s in the mixed system (Figures 4 and 6).

309 The difference between the PSD evolution of ambient sub-500 nm aerosols under electrostatic and Brownian
310 coagulation in a mixed system containing a dust fraction of 300 #/cm³ is modest but noticeable. As shown in
311 Figure 6, under Brownian coagulation the peak number concentrations at 100 and 1000 s are ~11000 and



312 7700 #/cm³, corresponding to diameters of 71 and 113 nm, whereas under the electrostatic coagulation at the
313 same times the peak number concentrations are ~10700 and 7100 #/cm³, with the peak diameter unchanged.
314 These changes in peak number concentration show a maximum difference of ~10%, indicating that dust
315 aerosols exert only a modest but noticeable influence on the PSD of ambient sub-500 nm aerosols. Although
316 the magnitude of this difference is modest compared with the much larger PSD differences observed for
317 highly charged dust aerosols, this ~10% difference might remain environmentally relevant.



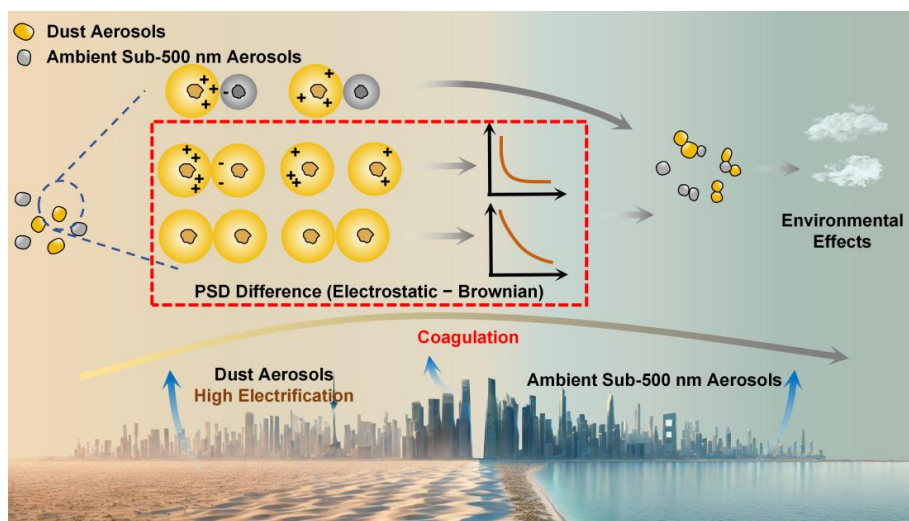
318

319 **Figure 6.** Temporal evolution of the PSD and total number concentration of ambient aerosols, containing a
320 dust aerosol fraction of 300 #/cm³, simulated at 25 °C. (a) PSD of ambient aerosols under Brownian
321 coagulation, with the dust fraction primarily concentrated in the size range greater than 0.5 μm . Curves
322 correspond to the times indicated in the legend. (b) PSD of ambient aerosols under electrostatic coagulation.
323 (c) Temporal evolution of total number concentrations of ambient sub-500 nm aerosols and dust aerosols
324 under Brownian coagulation. (d) Same as (c), but for electrostatic coagulation.

325 The rate of electrostatic coagulation between dust aerosols and ambient sub-500 nm aerosols first increases
326 and then decreases on hourly timescales. Specifically, during the early stage of electrostatic coagulation, the
327 number concentration of ambient sub-500 nm aerosols declines markedly faster than under Brownian
328 coagulation. However, by 10000 s, the peak number concentration under electrostatic coagulation is even
329 slightly higher than under Brownian coagulation (Figure 6a, b). Mechanistically, high initial dust aerosol
330 concentration increases collision frequency, and high charge enhances Coulomb interactions, which together
331 accelerate coagulation within dust and with ambient sub-500 nm aerosols. As time progresses, dust aerosol

332 concentration and charge decrease (Figure S9), thus reducing electrostatic coagulation with ambient sub-500
333 nm aerosols. This indicates that the electrostatic enhancement of coagulation between dust aerosols and
334 ambient sub-500 nm aerosols is strongly time-dependent and gradually diminishes during long-range
335 transport.

336 To summarize these processes, Figure 7 provides a conceptual comparison of the two coagulation
337 mechanisms. Enhanced Coulomb interactions among highly charged dust aerosols promote faster coagulation
338 and accelerate number concentration decay, while interactions with ambient sub-500 nm aerosols produce
339 smaller but still observable PSD changes. These results indicate that electrostatic effects may play an
340 important role in shaping aerosol size distributions and their atmospheric impacts.



341

342 **Figure 7.** Conceptual schematic illustrating the contrasting PSD evolution under electrostatic and Brownian
343 coagulation. The nonequilibrium bipolar high-charge state of dust aerosols enhances the effective coagulation
344 rate via Coulomb interactions, accelerating PSD evolution and number concentration decay. Highly charged
345 dust aerosols also modestly accelerate coagulation among ambient sub-500 nm aerosols.

346 4 Conclusions

347 Air quality models usually omit the charge term in the coagulation kernel, thereby neglecting Coulomb
348 interactions during collisions of charged aerosols. In this study, a dedicated DMA–APS configuration is used
349 to retrieve size-resolved single-particle charge distributions for dust aerosols, providing key inputs resolved
350 by particle size and charge amount to the coagulation model. For a dust-only scenario at typical
351 environmental concentrations (300 \#/cm^3), over 0–10000 s the PSD remains essentially unchanged under



352 Brownian coagulation, whereas under electrostatic coagulation the peak diameter shifts from ~ 0.9 to $1.5 \mu\text{m}$
353 and the peak number concentration decreases by $\sim 64\%$, demonstrating that the PSD evolution of dust aerosols
354 on hourly timescales clearly differs between Brownian and electrostatic coagulation. These results
355 demonstrate that Coulomb interactions can substantially influence the coagulation of highly charged aerosols
356 and must therefore be included explicitly in the coagulation kernel.

357 Given that dust aerosols in the atmosphere mix with abundant ambient sub-500 nm aerosols, it is necessary
358 to quantify how highly charged dust aerosols modify the PSD evolution of ambient aerosols under Brownian
359 versus electrostatic coagulation. When ambient sub-500 nm aerosols are introduced, dust PSD evolution
360 shows no detectable change relative to the dust-only scenario under both Brownian and electrostatic
361 coagulation. Electrostatic coagulation by dust aerosols exerts modest but measurable effects on ambient sub-
362 500 nm aerosols, leading to $\sim 10\%$ differences in peak number concentration relative to Brownian coagulation.

363 Overall, PSD evolution under electrostatic coagulation differs from Brownian coagulation and exhibits
364 pronounced temporal and spatial dependence in systems containing highly charged aerosols. These results
365 indicate that assessments of radiative effects, cloud droplet formation and aerosol deposition should explicitly
366 account for aerosol charge, particularly for highly charged aerosol populations.

367



368 **Code and data availability**

369 All data supporting the findings are archived at Mendeley Data (<https://doi.org/10.17632/n8ys5rzcty.1>). The
370 MATLAB analysis and simulation code and configuration files are included in the same Mendeley Data
371 record. Any additional information is provided in the Supplement. During peer review, access is provided
372 via the private Mendeley Data link; the record will be made public upon publication.

373 **Author contributions**

374 XW conceptualized the study, supervised the project, provided scientific guidance, and led the writing and
375 revision of the manuscript. XL revised and edited the manuscript. LQ conducted the experiments, processed
376 the data, developed the numerical model, and wrote the manuscript. RZ contributed to the construction of the
377 experimental setup, data processing, and the preliminary development of the model framework. All other co-
378 authors participated in the experiments and contributed to the discussion and revision of the manuscript.

379 **Competing interests**

380 The authors declare that they have no competing interests.

381 **Acknowledgements**

382 We thank R. Losno for sharing the SyGAVib design details.

383 **Financial support**

384 This work was supported by the National Natural Science Foundation of China (grant no. 42377090) and the
385 Shanghai Natural Science Foundation (grant no. 23ZR1479700).

386 **References**

387 Adachi, M., Okuyama, K., and Kousaka, Y.: Electrostatic coagulation of bipolarly charged aerosol particles,
388 Journal of Chemical Engineering of Japan, 14, 467–473, <https://doi.org/10.1252/JCEJ.14.467>, 1981.

389



390 Chen, S., Zhao, D., Huang, J., He, J., Chen, Y., Chen, J., Bi, H., Lou, G., Du, S., Zhang, Y., and Yang, F.:
391 Mongolia contributed more than 42% of the dust concentrations in northern China in March and April 2023,
392 *Advances in Atmospheric Sciences*, 40, 1549–1557, <https://doi.org/10.1007/s00376-023-3062-1>, 2023.

393 Cimarelli, C. and Genareau, K.: A review of volcanic electrification of the atmosphere and volcanic lightning,
394 *Journal of Volcanology and Geothermal Research*, 422, 107449,
395 <https://doi.org/10.1016/j.jvolgeores.2021.107449>, 2022.

396 Fuchs, N. A.: *The Mechanics of Aerosols*, Pergamon Press, Oxford, 1964.

397 Grell, G. A., Peckham, S. E., Schmitz, R., McKeen, S. A., Frost, G., Skamarock, W. C., and Eder, B.: Fully
398 coupled “online” chemistry within the WRF model, *Atmospheric Environment*, 39, 6957–6975,
399 <https://doi.org/10.1016/j.atmosenv.2005.04.027>, 2005.

400 Harrison, R. G. and Carslaw, K. S.: Ion–aerosol–cloud processes in the lower atmosphere, *Reviews of*
401 *Geophysics*, 41, 1012, <https://doi.org/10.1029/2002RG000114>, 2003.

402 Hoppel, W. A., Anderson, R. V., and Willett, J. C.: Atmospheric electricity in the planetary boundary layer,
403 in: *The Earth’s Electrical Environment*, 149–165, National Academy Press, Washington, D.C., 1986a.

404 Israel, H.: *Atmospheric Electricity*, Vol. 1, Israel Program for Scientific Translations, Jerusalem, distributed
405 by the National Science Foundation, Washington, D.C., 1970.

406 Israel, H.: *Atmospheric Electricity*, Vol. 2, Israel Program for Scientific Translations, Jerusalem, distributed
407 by the National Science Foundation, Washington, D.C., 1973.

408 Kok, J. F., Adebisi, A. A., Albani, S., Balkanski, Y., Checa-Garcia, R., Chin, M., Colarco, P. R., et al.:
409 Improved representation of the global dust cycle using observational constraints on dust properties and
410 abundance, *Atmospheric Chemistry and Physics*, 21, 8127–8167, <https://doi.org/10.5194/acp-21-8127-2021>,
411 2021.

412 Kumar, P., Morawska, L., Birmili, W., Paasonen, P., Hu, M., Kulmala, M., Harrison, R. M., Norford, L., and
413 Britter, R.: Ultrafine particles in cities, *Environment International*, 66, 1–10,
414 <https://doi.org/10.1016/j.envint.2014.01.013>, 2014.

415 Lee, Y. H., Chen, K., and Adams, P. J.: Development of a global model of mineral dust aerosol microphysics,
416 *Atmospheric Chemistry and Physics*, 9, 2441–2458, <https://doi.org/10.5194/acp-9-2441-2009>, 2009.

417 Li, Y., Chen, X., and Jiang, J.: Measuring size distributions of atmospheric aerosols using natural air ions,
418 *Aerosol Science and Technology*, 56, 655–664, <https://doi.org/10.1080/02786826.2022.2060795>, 2022.

419 Liu, B. Y. H. and Pui, D. Y. H.: Equilibrium bipolar charge distribution of aerosols, *Journal of Colloid and*
420 *Interface Science*, 49, 305–312, [https://doi.org/10.1016/0021-9797\(74\)90366-X](https://doi.org/10.1016/0021-9797(74)90366-X), 1974.

421 Ma, Xiewen, Gao, Qiangqian, Jiang, Xinghua, Chen, Shaodong, Gan, Yugi, Zhang, Tao, Lu, Xiaohui, and
422 Wang, Xiaofei.: Direct effects of air humidity on dust aerosol production: Evidence for the surprising role of



423 electrostatic forces, *Geophysical Research Letters*, 50, e2023GL103639,
424 <https://doi.org/10.1029/2023GL103639>, 2023.

425 Mallios, Sotirios A., Daskalopoulou, Vasiliki, and Amiridis, Vassilis.: Modeling of the electrical interaction
426 between desert dust particles and the Earth's atmosphere, *Journal of Aerosol Science*, 165, 106044,
427 <https://doi.org/10.1016/j.jaerosci.2022.106044>, 2022.

428 Maring, H., Savoie, D. L., Izaguirre, M. A., Custals, L., and Reid, J. S.: Mineral dust aerosol size distribution
429 change during atmospheric transport, *Journal of Geophysical Research: Atmospheres*, 108, 8592,
430 <https://doi.org/10.1029/2002JD002536>, 2003.

431 Morawska, L., Ristovski, Z., Jayaratne, E. R., Keogh, D. U., and Ling, X.: Ambient nano and ultrafine
432 particles from motor vehicle emissions: Characteristics, ambient processing and implications on human
433 exposure, *Atmospheric Environment*, 42, 8113–8138, <https://doi.org/10.1016/j.atmosenv.2008.07.050>, 2008.

434 Mu, Feifei and Fiedler, Stephanie.: How much do atmospheric depressions and Mongolian cyclones
435 contribute to spring dust activities in East Asia?, *npj Climate and Atmospheric Science*, 8, Article number
436 51, <https://doi.org/10.1038/s41612-025-00929-w>, 2025.

437 Oron, Alexander and Seinfeld, John H.: The dynamic behavior of charged aerosols: II. Numerical solution
438 by the sectional method, *Journal of Colloid and Interface Science*, 133, 66–79, [https://doi.org/10.1016/0021-9797\(89\)90282-8](https://doi.org/10.1016/0021-9797(89)90282-8), 1989.

440 Quan, L.: Critical Role of Dust Induced Electrostatic Coagulation in the Evolution of Aerosol Size
441 Distributions in the Atmosphere [Dataset], Mendeley Data, Version 1,
442 <https://data.mendeley.com/datasets/n8ys5rzcty/1>, 2026.

443 Pöschl, U.: Atmospheric aerosols: Composition, transformation, climate and health effects, *Angewandte*
444 *Chemie International Edition*, 44, 7520–7540, <https://doi.org/10.1002/anie.200501122>, 2005.

445 Qu, Zhiqiang, Trabelsi, Zied A., Losno, Roseline, Monna, Fabrice, Nowak, Stephan, Masmoudi, Mohamed,
446 and Quisefit, Jean-Paul.: A laboratory dust generator applying vibration to soil sample: Mineralogical study
447 and compositional analyses, *Journal of Geophysical Research: Atmospheres*, 125, e2019JD032224,
448 <https://doi.org/10.1029/2019JD032224>, 2020.

449 Ramnarine, E., Kodros, J. K., Hodshire, A. L., Lonsdale, C. R., Alvarado, M. J., and Pierce, J. R.: Effects of
450 near-source coagulation of biomass-burning aerosols on global predictions of aerosol size distributions and
451 implications for aerosol radiative effects, *Atmospheric Chemistry and Physics*, 19, 6561–6577,
452 <https://doi.org/10.5194/acp-19-6561-2019>, 2019.

453 Rose, C., Collaud Coen, M., Andrews, E., Lin, Y., Bossert, I., Lund Myhre, C., Tuch, T., Wiedensohler, A.,
454 Fiebig, M., Aalto, P., et al.: Seasonality of the particle number concentration and size distribution: A global



455 analysis retrieved from the network of Global Atmosphere Watch (GAW) near-surface observatories,
456 Atmospheric Chemistry and Physics, 21, 17185–17223, <https://doi.org/10.5194/acp-21-17185-2021>, 2021.
457 Shao, J. and Mao, J.: Dust particle size distributions during spring in Yinchuan, China, Advances in
458 Meteorology, 2016, Article ID 4050240, <https://doi.org/10.1155/2016/6940502>, 2016.
459 Tammet, H., Hörrak, U., Laakso, L., and Kulmala, M.: Factors of air ion balance in a coniferous forest
460 according to measurements in Hyytiälä, Finland, Atmospheric Chemistry and Physics, 6, 3377–3390,
461 <https://doi.org/10.5194/acp-6-3377-2006>, 2006.
462 Tegen, I. and Lacis, A. A.: Modeling of particle size distribution and its influence on the radiative properties
463 of mineral dust aerosol, Journal of Geophysical Research: Atmospheres, 101, 19237–19244,
464 <https://doi.org/10.1029/95JD03610>, 1996.
465 Tiggens, L., Wiedensohler, A., Weinhold, K., Gandhi, J., and Schmid, H.-J.: Bipolar charge distribution of a
466 soft X-ray diffusion charger, Journal of Aerosol Science, 90, 77–86,
467 <https://doi.org/10.1016/j.jaerosci.2015.07.002>, 2015.
468 Xie, H., Wang, Z., Luo, T., Yang, K., Zhang, D., Zhou, T., Yang, X., Liu, X., and Fu, Q.: Seasonal variation
469 of dust aerosol vertical distribution in Arctic based on polarized micropulse lidar measurement, Remote
470 Sensing, 14, 5581, <https://doi.org/10.3390/rs14215581>, 2022.
471 Zebel, G.: Zur Theorie des Verhaltens elektrisch geladener Aerosole, Kolloid-Zeitschrift., 157, 37–50, 1958.
472 Zhang, H. and Zhou, Y.-H.: Reconstructing the electrical structure of dust storms from locally observed
473 electric field data, Nature Communications, 11, 5072, <https://doi.org/10.1038/s41467-020-18759-0>, 2020.
474 Zhang, R., Lu, X., Wang, L., Chen, J., Chen, D.-R., and Wang, X.: Extremely inexpensive and simple method
475 to remove indoor respiratory aerosols, Environmental Science & Technology Letters, 10, 786–791,
476 <https://doi.org/10.1021/acs.estlett.3c00541>, 2023.
477